International Journal of Heat and Mass Transfer 159 (2020) 120128

Contents lists available at ScienceDirect

International Journal of Heat and Mass Transfer

journal homepage: www.elsevier.com/locate/hmt

Numerical investigation of spatial-developing turbulent heat transfer in forced convections at different supercritical pressures

Jiaming Liu[b], Pinghui Zhao[a,*], Mingzhun Lei[a], Suo Yang[c], Hassan Nemati[d]

[a] Institute of Plasma Physics Chinese Academy of Science, Hefei, Anhui 230031, China
[b] School of Nuclear Science and Technology, University of Science and Technology of China, Hefei, Anhui 230026, China
[c] Department of Mechanical Engineering, University of Minnesota - Twin Cities, Minneapolis, MN 55455, United States
[d] Department of Process & Energy, Delft University of Technology, 2628CB Delft, Netherlands

ARTICLE INFO

Article history:
Received 31 March 2020
Revised 15 June 2020
Accepted 25 June 2020
Available online 8 July 2020

Keywords:
Turbulent heat transfer
Supercritical pressure
Spatial-developing flow
Direct numerical simulation

ABSTRACT

Direct numerical simulations have been adopted to study the turbulent heat transfer in forced convections of supercritical water at two different supercritical pressures P=23 MPa and P=25 MPa in a heated pipe with constant wall heat flux and a bulk Reynolds number of $Re_0 = 5400$. The present study aims to reveal the mechanisms of turbulent heat transfer of supericritical fluids at different pressures in a spatial-developing flow. The results show that at the smaller pressure ratio $P_r = P/P_c$, where P_c is the critical pressure, the property variations become more drastic, and both the skin friction coefficient and Nusselt number become smaller. The decompositions of skin friction and Nusselt number show that it is mainly due to the large turbulence reduction along the streamwise direction. The analyses of turbulent kinetic energy (TKE), the turbulent shear stress, and the production of TKE confirm this point. Moreover, it was found that the thermophysical property fluctuations are very large and significantly influence the turbulent statistics in the supercritical fluid flows. Due to the large property fluctuations, it was found that the density-fluctuation-related terms are significant and their values are actually comparable to the mean-density-related terms. Due to their negative contributions to turbulent shear stress and turbulent heat flux, the turbulence and heat transfer are severely attenuated by the large thermophysical property fluctuations. For near-wall scaling in spatial-developing flows at supercritical pressures, the semi-local velocity transformation with a semi-local coordinate shows a better agreement in the logarithmic region. However, a clear deviation still exists, especially for mean temperature because all the transformations only incorporate the local mean property variations and cannot consider their fluctuations.

1. Introduction

A supercritical water-cooled reactor (SCWR) has been selected as one of the candidates for the Generation IV reactor system due to its high economy, low flow rate, single-phase water-cooling, high enthalpy rise, and a simplified system [1]. When water with continuous heating flows through the reactor core at supercritical pressures, it experiences a special process from a liquid-like state to a gas-like state, which leads to peculiar property variations, including density ρ, dynamic viscosity μ, specific heat c_p and thermal conductivity λ, near the pseudo-critical temperature T_{pc}. When the system pressure becomes close to the critical pressure, water properties exhibit sharper variation, especially for thermal conductivity, specific heat and Prandtl number. As shown in Fig. 1, an obvious difference of property variations of water under the two different pressures can be observed. Owing to their different property variations, turbulence and heat transfer behaviors show much difference between each other.

Experimental and numerical investigations of heat transfer behavior of supercritical fluids at supercritical pressures have been conducted since the 1960s. Pioro et al. [2,3] have summarized many experimental studies for the turbulent heat transfer of supercritical water in channels. From these experiments, Swenson et al. [4] and Yamagata et al. [5] found that the peaks of heat transfer coefficient (HTC) gradually decrease with the increase of pressures. Bae [6] studied the mixed convective heat transfer of supercritical carbon dioxide (sCO_2) in vertical heat pipes and annular channels by experiments. Wang et al. [7,8] also found that the peaks of HTC decrease when the pressures are close to the critical pressure. Moreover, Zhao et al. [9] conducted some experimental studies in heated pipes and annuli, and found that the peaks of HTC are higher with pressures closer to critical pressure due

* Corresponding author.
E-mail address: phzhao@mail.ustc.edu.cn (P. Zhao).

https://doi.org/10.1016/j.ijheatmasstransfer.2020.120128
0017-9310/

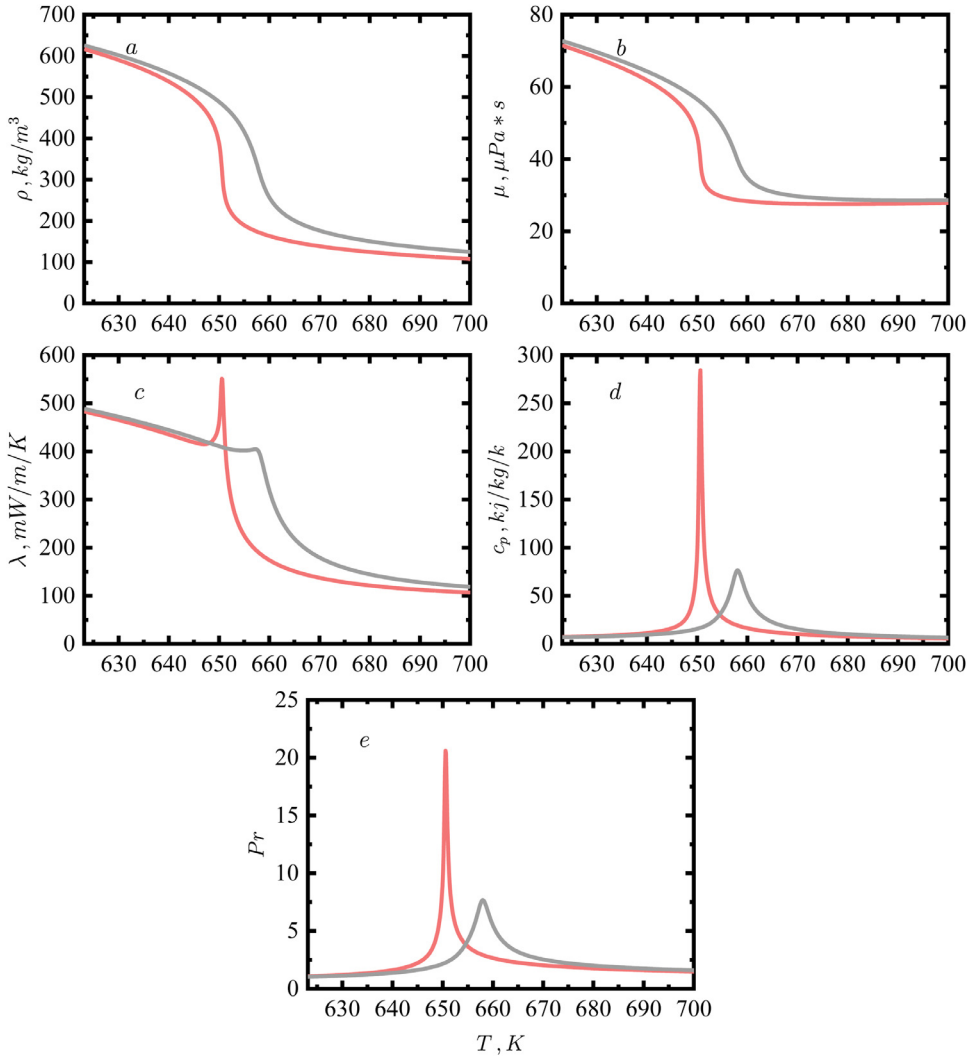

Fig. 1. The thermophysical property of water as a function of temperature; a: density ρ; b: dynamic viscosity μ; c: thermal conductivity λ; d: specific heat c_p; e: Prandtl number Pr. Red line: 23 MPa, $T_{pc} = 650.60\ K$; gray line: 25 MPa, $T_{pc} = 658.05\ K$.

to larger property variations. In their opinions, the higher Prandtl number and lower pseudo-critical temperature are responsible for the phenomenon. Gu et al. [10] also carried out some experimental studies to investigate the heat transfer of supercritical water in pipes at high heat fluxes. They found that higher Prandtl number at low pressure leads to larger HTC. Liu et al. [11] also conducted some experiments on heat transfer of sCO_2 in cooling tubes. From their results, it was found that heat transfer coefficient increases greatly due to decreasing inlet pressures. Huang et al. [12] studied the heat transfer of aviation kerosene in vertical pipes by experiments. In their opinions, higher viscosity and thermal conductivity induced by increasing pressures lead to large heat transfer coefficient and enhanced heat transfer. Though the experiments show that large property variations of supercritical fluids have a significant effect on the turbulence and heat transfer, the mechanism is still not clear due to the difficulty of experimental measurements.

Due to the limitations of conventional Reynolds Averaged Navier-Stokes (RANS) and Large Eddy Simulation (LES) models, direct numerical simulations (DNS) is recommended as a powerful method to provide more insights into turbulent and thermal physics. Instead of modeling turbulence, DNS method directly solves the turbulence at all scales, providing the most detailed turbulence data and a deeper physical interpretation of the turbulent heat transfer at supercritical pressures. Based on DNS, Bae et al. [13,14] investigated the turbulent heat transfer of sCO_2 flowing in a heated vertical pipe and annulus. Turbulent statistics, such as turbulent shear stress, turbulent kinetic energy (TKE), turbulent heat flux and the production of TKE, etc., were analyzed to reveal the turbulent heat transfer behavior at supercritical pressures. Nemati et al. [15] used DNS to investigate the mean statistics of sCO_2 and the effect of thermal boundary conditions in a developing pipe flow. In their work, they found that the Nusselt number shows a reduction when the temperature fluctuations at the wall are suppressed. Chu et al. [16] carried out the studies of flow stratification of sCO_2 in a heated horizontal pipe. Using DNS, Pandey et al. [17] conducted five cases to demonstrate the buoyancy-induced turbulent modulation of sCO_2 under cooling conditions. Peeters et al. [18,19] studied the characteristics of turbulent heat transfer and turbulence attenuation of sCO_2 in a fully developed annulus. In the latest DNS studies, Kawai [20] found that large thermophysical property variations near the wall lead to significant near-wall density fluctuations, which further changes the velocity profiles in a fully developed boundary layer flow. However, the previous DNS analyses mainly focused on the effects of different inlet velocities and wall heat fluxes on the turbulent heat transfer at a fixed supercritical pressure. As shown in Fig. 1, the property variations change greatly with different supercritical pressures, which may influence the turbulence and heat transfer significantly. Therefore,

the mechanisms of different pressures on the turbulent heat transfer of supercritical fluids should be comprehensively studied by DNS.

In this work, we investigate the turbulent heat transfer at different supercritical pressures by performing DNS of a spatial-developing pipe flow. Thermophysical properties, skin friction coefficient, Nusselt number, turbulent statistics and FIK decompositions etc. were employed to demonstrate the characteristics of spatial-developing heat transfer of supercritical fluids. Flow visualization was also applied to display the effects of pressure variation on the coherent structures.

2. Numerical methodology

A detailed description of the DNS method can be found in our previous work [21]. A brief description of governing equations and numerical methods is provided here. The DNS code has been thoroughly validated by experiment data of a strong-heated air pipe flow with variable properties [21] and DNS data of constant property flows [22]. More details of the code validation can be found in Appendix A.

2.1. Governing equations and numerical methods

In this study, the Navier-Stokes equations with the low-Mach approximations were employed. Such an approximation has been applied to the DNS study of turbulent heat transfer of supercritical fluids by Bae et al. [13], Chu et al. [16], Nemati et al. [15], Peeters et al. [19] and Liu et al. [23].

Continuity equation:

$$\frac{\partial \rho}{\partial t}+\frac{\partial\left(\rho u_j\right)}{\partial x_j}=0, \tag{1}$$

Momentum equations:

$$\frac{\partial\left(\rho u_i\right)}{\partial t}+\frac{\partial\left(\rho u_i u_j\right)}{\partial x_j}=-\frac{\partial p}{\partial x_i}+\frac{\partial \tau_{ij}}{\partial x_j}, \tag{2}$$

Energy equation:

$$\frac{\partial(\rho h)}{\partial t}+\frac{\partial\left(\rho u_j h\right)}{\partial x_j}=-\frac{\partial q_j}{\partial x_j} \tag{3}$$

where

$$\tau_{ij}=2\frac{\mu}{Re}\left(S_{ij}-\frac{1}{3}\delta_{ij}\frac{\partial u_k}{\partial x_k}\right),\ S_{ij}=\frac{1}{2}\left(\frac{\partial u_i}{\partial x_j}+\frac{\partial u_j}{\partial x_i}\right),$$
$$q_i=-\frac{k}{RePr}\frac{\partial T}{\partial x_i}=-\frac{1}{RePr}\frac{k}{c_p}\frac{\partial h}{\partial x_i}. \tag{4}$$

In Eqs. (1)–(3), all the variables are nondimensionalized and those parameters are derived as follows:

$$x_i=\frac{x_i^*}{R},\ t=\frac{t^*U_0}{R},\ u_i=\frac{u_i^*}{U_0},\ p=\frac{p^*}{\rho_0U_0^2},\ \rho=\frac{\rho^*}{\rho_0},\ \mu=\frac{\mu^*}{\mu_0},\ k=\frac{k^*}{k_0},$$
$$c_p=\frac{c_p^*}{c_{p0}},\ T=\frac{T^*}{T_0},\ h=\frac{h^*-h_0}{c_{p0}T_0}Re=\frac{\rho_0U_0R}{\mu_0},\ Q^+=\frac{q_wR}{k_0T_0}=RePrq^+,$$
$$q^+=\frac{q_w}{\rho_0U_0c_{p0}T_0}. \tag{5}$$

Where the subscript 0 refers to the inlet condition, the superscript * denotes dimensional quantities. In Eqns. (1)-(3), ρ represents density, u_i denotes the component of the velocity vector, p is pressure, h is enthalpy, T is temperature, R is radius, U_0 indicates inlet bulk velocity. Details of this non-dimensional method can be found in our previous paper [23]. The thermophysical properties of water at different supercritical pressures were derived from NIST REFPROP [24] and further interpolated during the computational process. The property variations at 23 MPa close to the H_2O critical pressure 22.1 MPa are obviously more drastic than 25 MPa as shown in Fig. 1.

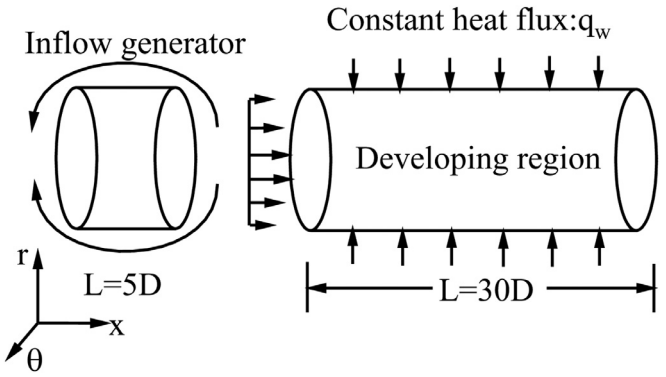

Fig. 2. The flow schematic of the present direct numerical simulation.

Table 1
Summary of computational setups.

Case	P(MPa)	Re_0	N_x	N_r	N_θ	Δx^+	Δr^+	$R\Delta\theta^+$
A	23	5400	1960	166	256	5.6	0.08–3.40	4.75
B	25	5400	1536	162	256	7.1	0.08–3.48	4.75
C	–	5400	1536	130	256	7.1	0.12–3.56	4.75

2.2. Computational setups

The present computational domain includes an inflow generator and a spatial-developing region with constant heat flux at the wall, as shown in Fig. 2. The size of inflow generator and developing region is $L_{in}=5D$ and $L_d=30D$, respectively, in the streamwise (x) direction. The inflow generator has a resolution of 128 × 256 × 256 (radial r, axial x, and circumferential θ directions), which provides a fully developed turbulent velocity for the inlet of the developing region. The inlet temperature is set as a constant value of 623.15 K and inlet bulk velocity U_0 is 0.314 m/s for all the cases. The details of the computational setups are presented in Table 1. For convenience, a constant property flow, case C, was chosen for the comparison. In general, the minimum thermal scale is smaller than the Kolmogorov microscale because of the Prandtl number $Pr > 1.0$ at supercritical pressures. Therefore, both the Kolmogorov microscales $\eta_k=((\bar{\nu})^3/\varepsilon)^{0.25}$ and the smallest scales of the temperatures $\eta_\theta=\eta_k/Pr^{-0.5}$ were illustrated at different streamwise positions in Fig. 3(a)–3(f), where ε is the dissipation rate of TKE. From Fig. 3, the mesh resolutions with y (y = 1-r) as the horizontal coordinate in three directions are well resolved. The present mesh resolutions of thermal scales are $1.0<\Delta x/\eta_\theta<2.5$, $1.5<\Delta x/\eta_\theta<8.3$ in the axial direction for case A and B, respectively, $0.05<\Delta r/\eta_\theta<0.7$ in the radial direction for all cases, and $1.0<\Delta\theta/\eta_\theta<1.9, 1.25<\Delta\theta/\eta_\theta<5.2$ in the circumferential direction for case A and B, respectively. The present mesh resolutions meet the resolution requirements in this study. In a prior DNS studies, Zonta et al. [25], Jin et al. [26], Nemati et al. [27] and Kawai [20] have also reported comparable mesh resolutions.

3. Results and discussions

In this section, the characteristics of spatial-developing turbulent heat transfer at different supercritical pressures will be

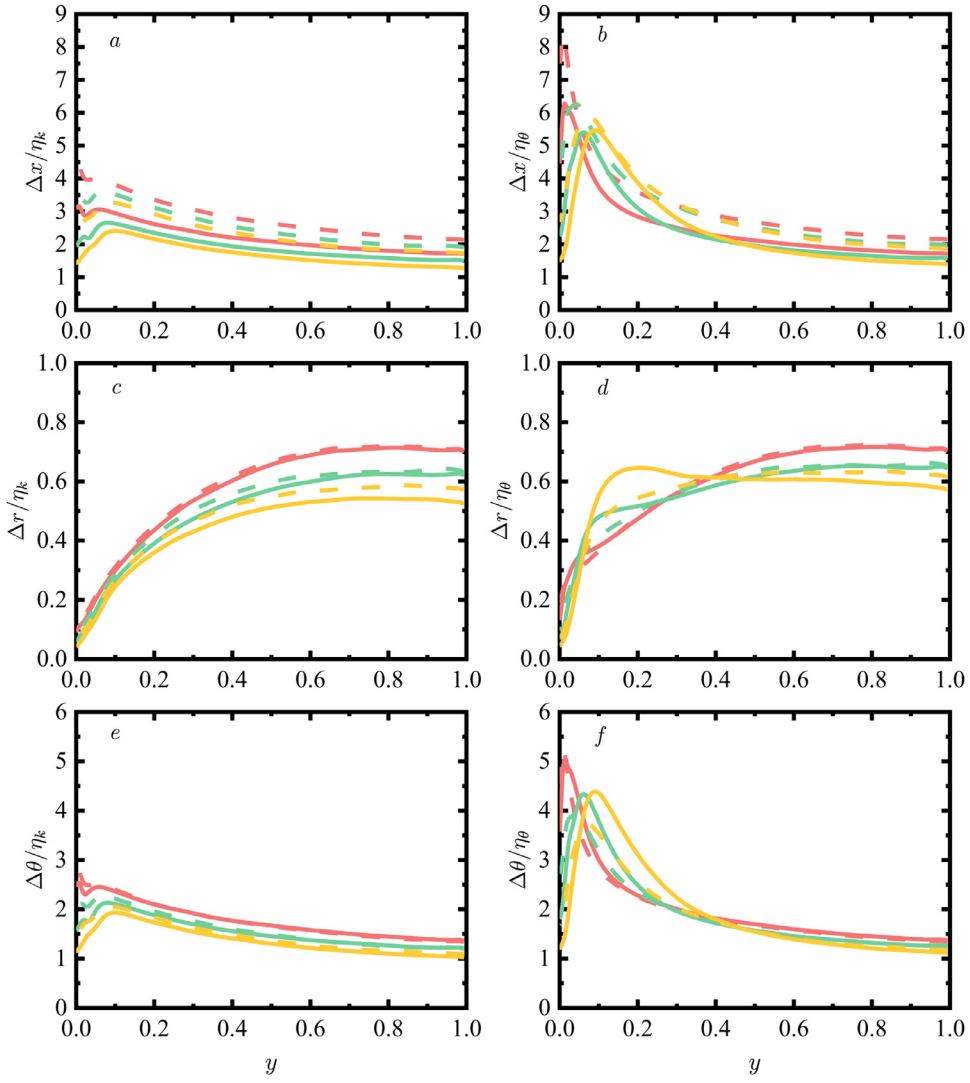

Fig. 3. Kolmogorov microscale η_k (a, c, e) and the smallest scale of the temperature field η_θ (b, d, f) at different streamwise locations. Red: $X = 15$; green: $X = 35$; yellow: $X = 55$, solid line: $P = 23$ MPa; dashed line: $P = 25$ MPa. (For interpretation of the references to colour in this figure legend, the reader is referred to the web version of this article.)

discussed. For an arbitrary instantaneous variable, φ, it can be decomposed into a Reynolds averaged variable $\bar{\varphi}$ and its fluctuation φ', where $\varphi = \bar{\varphi} + \varphi'$ with $\overline{\varphi'} = 0$, or into Favred averaged variable $\tilde{\varphi}$ and its fluctuation φ'', where $\varphi = \tilde{\varphi} + \varphi''$ with $\overline{\rho\varphi''} = 0$. These two kinds of averaging are related as follows:$\tilde{\varphi} = \overline{\rho\varphi}/\bar{\rho}$, $\overline{\varphi''} = -\overline{\rho'\varphi'}/\bar{\rho} \neq 0$. The dimensionless time step for the present study was set to $\Delta t = 0.25$ under a maximum Courant number of 0.8. The turbulent statistics were obtained by time-averaging over at least 10,000 time steps, which corresponds to 30 flow times of the computational region.

3.1. Mean quantity profiles

In Fig. 4(a)–4(b), wall temperature T_w and flow acceleration parameter $K_v = \frac{\bar{\nu}}{U_b^2}\frac{dU_b}{dx}$, where U_b is the bulk mean velocity, are presented. As seen, a much larger wall temperature T_w can be observed in the cases at supercritical pressures than in constant property case C. Moreover, when comparing case A to case B, the increase of wall temperatures becomes faster with the supercritical pressure close to critical pressure. Here, we defined the pressure ratio $P_r = P/P_c$, which reflects the extent to which the supercritical pressure P deviates from the critical pressure P_c. Likewise, a larger flow acceleration parameter K_v can be observed in case A due to the more drastic density variation as shown in Fig. 1. However, for the present simulations, the parameter K_v ranged from about 0.75×10^{-6} to 1.10×10^{-6} which is smaller than the referenced value of $K_v \approx 1.5 \times 10^{-6}$ under which the flow acceleration is not important to turbulence as proposed by Chambers et al. [28].

In Fig. 5, the skin friction coefficient $C_f = 2(\overline{\mu_w}\partial\bar{u}/\partial y)/(\rho_b U_b^2)$ and Nusselt number $Nu = hD/k_b^*$, where $h = q_w/(T_w^* - T_b^*)$ is the convective heat coefficient, along the streamwise direction are shown. It can be found that the large property variations at supercritical pressures lead to the skin friction and Nusselt number decrease. Especially for the skin friction coefficient, where its decrease is remarkable along the streamwise direction compared to the constant property case. With the development of the turbulent boundary layer, the reduction of skin friction coefficient and Nusselt number becomes more obvious in case A when compared to case B. To comprehensively show the reason, a decomposition method of skin friction coefficient or Nusselt number originally developed by Fukagata, Iwamoto & Kasagi (FIK) was re-derived and applied in the following analyses of Section 3.2.

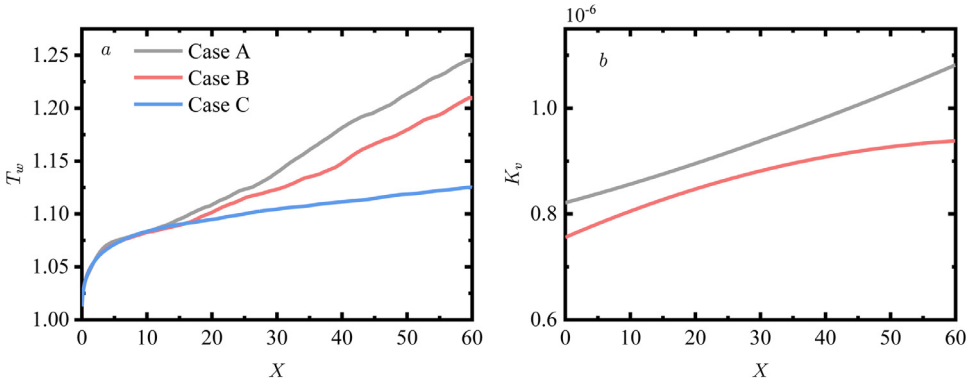

Fig. 4. Wall temperature T_w (a) and local flow acceleration parameter K_v (b) profiles.

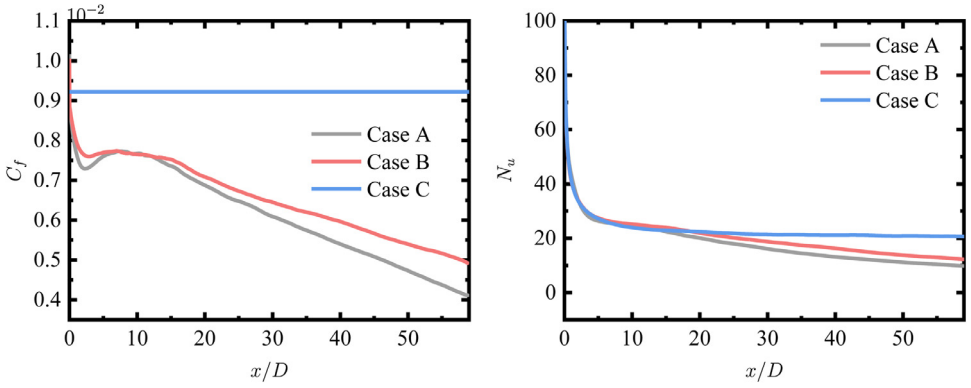

Fig. 5. The skin friction coefficient and Nusselt number.

3.2. Decompositions of skin friction coefficient and nusselt number

The decomposition method was firstly derived by Fukagata et al. [29] to investigate the individual contributions to the skin friction. Ever since, it has been widely used to study the turbulence effects on the skin friction and wall heat transfer in different flows such as fully developed channel and pipe flows [30], compressible flows [31], developing turbulent boundary layers [32], strong heated air flows [21], cooled or heated supercritical fluid flows [17].

In this study, we further re-derive the FIK identity to include the effect of property variations in supercritical fluids by the integration of the mean streamwise momentum and enthalpy equations twice in the radial direction. The derived FIK decompositions of skin friction coefficient and Nusselt number are as follows:

$$\begin{aligned}
C_{f,FIK} = &-\frac{16}{\rho_b u_b^2 Re_{b0}}\int_0^1 r\bar{\mu}\overline{S_{rx}}rdr+\frac{8}{\rho_b u_b^2}\int_0^1 r\overline{\rho u''_r u''_x}rdr\\
&+\frac{4}{\rho_b u_b^2}\int_0^1\left(1-r^2\right)<\frac{\partial\overline{P}}{\partial x}>rdr+\frac{4}{\rho_b u_b^2}\int_0^1 r\bar{\rho}\tilde{u}_r\tilde{u}_x rdr\\
&+\frac{8}{\rho_b u_b^2}\int_0^1\left(1-r^2\right)\left\langle\frac{\partial\bar{\rho}\tilde{u}_x\tilde{u}_x}{\partial x}\right\rangle rdr\\
&+\frac{4}{\rho_b u_b^2}\int_0^1\left(1-r^2\right)\left\langle\frac{\partial\overline{\rho u''_x u''_x}}{\partial x}\right\rangle rdr\\
&-\frac{8}{\rho_b u_b^2 Re_{b0}}\int_0^1\left(1-r^2\right)\left\langle\frac{1}{r}\frac{\partial\overline{\mu' S'_{rx}}}{\partial r}\right\rangle rdr\\
&-\frac{8}{\rho_b u_b^2 Re_{b0}}\int_0^1\left(1-r^2\right)\left\langle\frac{\partial\bar{\mu}\overline{S_{xx}}}{\partial x}\right\rangle rdr\\
&-\frac{8}{\rho_b u_b^2 Re_{b0}}\int_0^1\left(1-r^2\right)\left\langle\frac{\partial\overline{\mu' S'_{xx}}}{\partial x}\right\rangle rdr,
\end{aligned}\tag{6}$$

$$\begin{aligned}
Nu_{FIK} = &\frac{8}{\alpha_b\left(\overline{h_w}-h_b\right)}\int_0^1 r\bar{\alpha}\frac{\partial\tilde{h}}{\partial r}rdr-\frac{8Re_{b0}Pr_0}{\alpha_b\left(\overline{h_w}-h_b\right)}\int_0^1 r\overline{\rho h'' u''_r}rdr\\
&-\frac{4Re_{b0}Pr_0}{\alpha_b\left(\overline{h_w}-h_b\right)}\int_0^1\left(1-r^2\right)\left\langle\frac{1}{r}\frac{\partial r\bar{\rho}\tilde{h}\tilde{u}_r}{\partial r}\right\rangle rdr\\
&-\frac{4Re_{b0}Pr_0}{\alpha_b\left(\overline{h_w}-h_b\right)}\int_0^1\left(1-r^2\right)\left\langle\frac{\partial\bar{\rho}\tilde{h}\tilde{u}_x}{\partial x}\right\rangle rdr\\
&-\frac{4Re_{b0}Pr_0}{\alpha_b\left(\overline{h_w}-h_b\right)}\int_0^1\left(1-r^2\right)\left\langle\frac{\partial\overline{\rho h'' u''_x}}{\partial x}\right\rangle rdr\\
&+\frac{4}{\alpha_b\left(\overline{h_w}-h_b\right)}\int_0^1\left(1-r^2\right)\left\langle\frac{1}{r}\frac{\partial r}{\partial r}\overline{\alpha' h'}\right\rangle rdr\\
&+\frac{4}{\alpha_b\left(\overline{h_w}-h_b\right)}\int_0^1\left(1-r^2\right)\left\langle\frac{\partial}{\partial x}\left(\bar{\alpha}\overline{\frac{\partial h'}{\partial x}}\right)\right\rangle rdr\\
&+\frac{4}{\alpha_b\left(\overline{h_w}-h_b\right)}\int_0^1\left(1-r^2\right)\left\langle\frac{\partial}{\partial x}\left(\overline{\alpha'\frac{\partial h'}{\partial x}}\right)\right\rangle rdr,
\end{aligned}\tag{7}$$

Here $\langle\ \rangle$ stands for:

$$\langle\varphi(r,z)\rangle=\varphi(r,z)-2\int_0^1\varphi(r,z)rdr.\tag{8}$$

In Equation (6), the skin friction coefficient was decomposed into the laminar contribution $C_{f,1}$ which is the first term on the right, the turbulent contribution $C_{f,2}$ which is the second term on the right, and inhomogeneous contribution $C_{f,inhomo}$ which is the sum of other terms. Eq. (7) shows the decomposed Nusselt number where the first term on the right stands for the laminar contribution Nu_1, the second term standing for the turbulent contribution

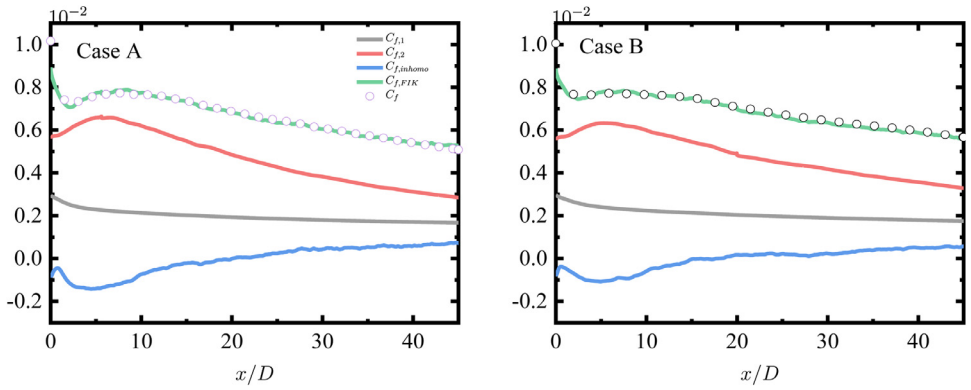

Fig. 6. The componential contributions to the skin friction. The symbol is DNS data, dash line is from case C.

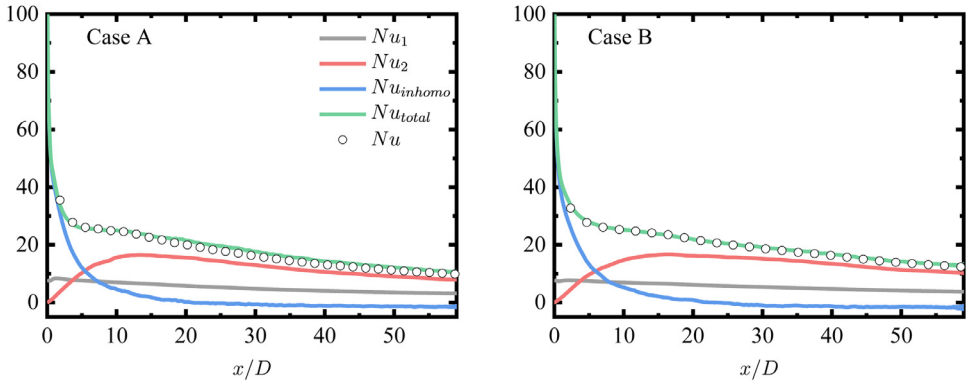

Fig. 7. The componential contributions to the Nusselt number. The symbol is DNS data, dash line is from case C.

Nu_2, and the sum of other terms standing for inhomogeneous contribution Nu_{inhomo}.

Fig. 6 plots the componential contributions to skin friction. In order to verify the present derivation, $C_{f,\,FIK}$, which is the sum of $C_{f,\,1}, C_{f,\,2}$ and $C_{f,\,inhomo}$, is compared firstly with the skin coefficient locally calculated by $C_f = 2\tau_w/\rho_b/U_b^2$. An excellent agreement is observed, ensuring the correctness and consistency. Along the streamwise direction, both the laminar and the non-homogenous contributions have experienced a small decrease due to the flow acceleration, while the turbulent contribution has seen a notable decrease. This means that the decrease of skin friction coefficients mainly results from the turbulence reduction. Furthermore, with the smaller pressure ratio, the turbulent contribution decreases even faster.

Fig. 7 shows the componential contributions to the Nusselt number in case A and B. To verify the decomposition, the locally calculated Nusselt number $Nu_b = h_c D/k_b^*$ is also compared with the FIK identity Nu_{FIK}. An excellent agreement can be observed, ensuring the correctness and consistency of the derivation. It can be seen in Fig. 7 that from inlet to $x = 10$, the inhomogenous contribution is a dominant effect on the total Nussult number due to the quickly developing thermal boundary layer, since the constant temperature inlet boundary condition is used in our simulations. After that, the turbulent contribution is dominant like the decomposition of skin friction coefficient. Similarly, both the laminar and inhomogenous contributions are relatively small and almost constant along the streamwise direction, while the turbulent contribution is important and obviously decreases due to turbulence reduction. Therefore, the conclusion can be drawn that the skin friction coefficient and Nusselt number decrease because of the turbulence reduction at supercritical pressures and smaller the pressure ratio, greater the turbulence reduction.

3.3. Turbulence statistics

From above analyses, the reduction of turbulent contribution leads to the decrease of the skin friction coefficient and Nusselt number. In order to further explore the reason of the turbulent reduction along the streamwise direction, the turbulence statistics such as Reynolds shear stress, turbulent kinetic energy (TKE), production of TKE and turbulent heat flux are shown in this section.

Fig. 8 shows the profiles of Reynolds shear stress $\overline{\rho u_x'' u_r''}/\tau_{w,0}$, TKE $-1/2(\overline{\rho u_i'' u_i''})/\tau_{w,0}$ and production of TKE $(P_k = -\overline{\rho u_i'' u_j''}(d\tilde{u}_j/dx_i))$. Along the streamwise direction, Reynolds shear stresses, TKE and production of TKE all decrease due to the turbulent reduction. Therefore, as described above, the turbulent contribution to skin friction coefficient and Nusselt number gradually reduces in the downstream. Comparing case A with case B, a quicker decrease of Reynolds shear stress, TKE as well as production of TKE is found in case A than in case B, which confirms that more turbulence reduction happens with the smaller pressure ratio.

Fig. 9 shows the profiles of axial $\overline{\rho u_x'' h''}/q^+$ and radial $\overline{\rho u_r'' h''}/q^+$ turbulent heat flux along streamwise direction. Along the streamwise direction, the axial turbulent heat fluxes gradually increase. This is due to the increase of the enthalpy fluctuations downstream, although velocity fluctuations actually decrease. The radial turbulent heat fluxes experience a small decrease downstream, which results in a slow reduction of turbulent contribution to the Nusselt number as described in Section 3.2.

3.4. Turbulent structures

In this section, we utilize the flow visualization technology to show the instantaneous turbulence along the streamwise direction.

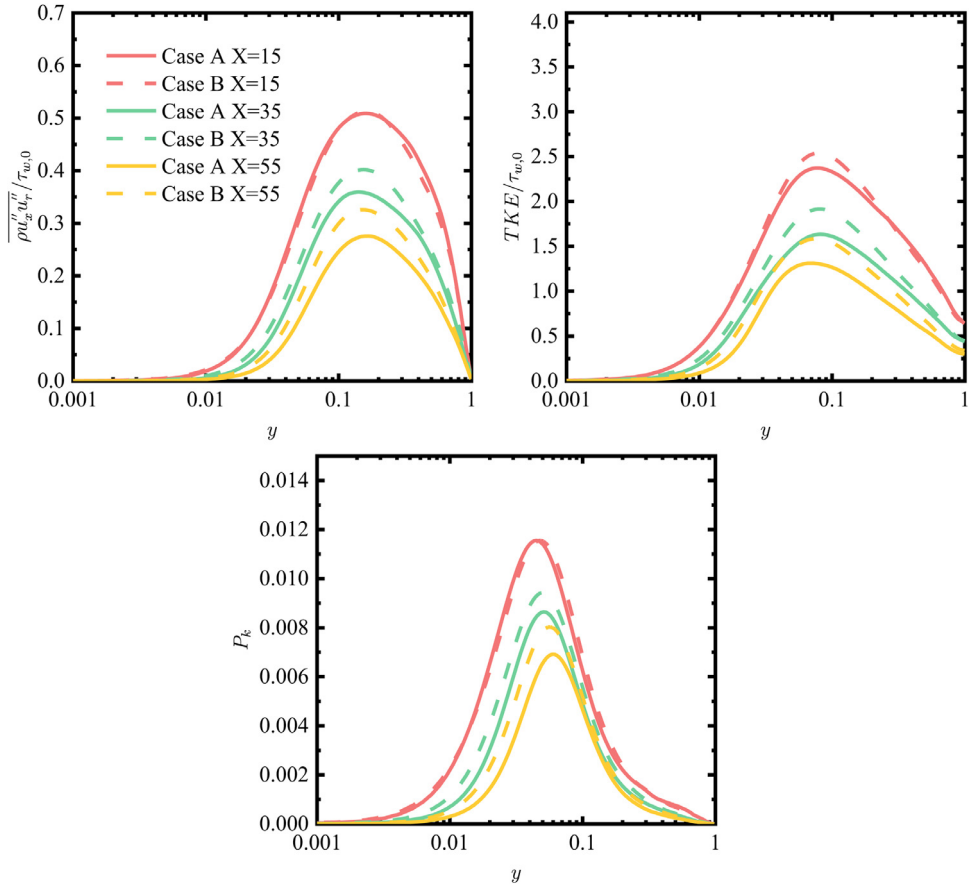

Fig. 8. Reynolds shear stress, turbulent kinetic energy (TKE) and production of TKE.

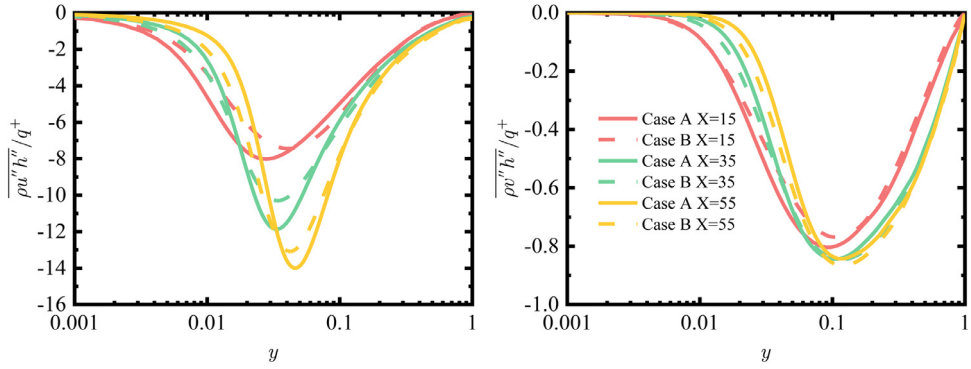

Fig. 9. The axial turbulent heat flux and radial turbulent heat flux.

In order to reveal the turbulent coherent structures clearly, only a part of the circumference is displayed near the wall region. In Fig. 10, the instantaneous velocity fluctuation at $y = 0.05$ ($y^+ \approx 10$) is shown. It can be found that in the downstream, the low-speed streaks become bigger and longer, and high-speed streaks become smaller and shorter. This means the turbulence is more anisotropic downstream. The presence of less high- and low-speed steaks mean that turbulence is attenuated in the downstream. Fig. 11 displays the instantaneous density fluctuation. Contrary to the streamwise velocity fluctuation, the density fluctuation continually increases in the downstream. Obviously, the density fluctuation is larger in case A than case B due to the smaller pressure ratio. The variation of instantaneous enthalpy fluctuation is similar to the density fluctuation.

3.5. Thermophysical property fluctuations

Fig. 12 shows the profiles of density fluctuation $\sqrt{\overline{\rho''\rho''}}/\bar{\rho}$ and Prandtl number fluctuation $\sqrt{\overline{Pr''Pr''}}/\overline{Pr}$ in the spatial-developing turbulent flow. It was found that the peak values of density fluctuation are larger than 0.5 and those of Prandtl number fluctuations are larger than 1.0. This is distinctly different from turbulent heat transfer in other flows such as strong heated air flows [21] or supersonic flows [33] in which the property fluctuation is less than 0.1 and when Morkovin's hypothesis is valid. Therefore, at supercritical pressures, the large property fluctuations may significantly modify the turbulence and their influence on heat transfer requires further study. In the following Sections 3.6 and 3.7, the effects of

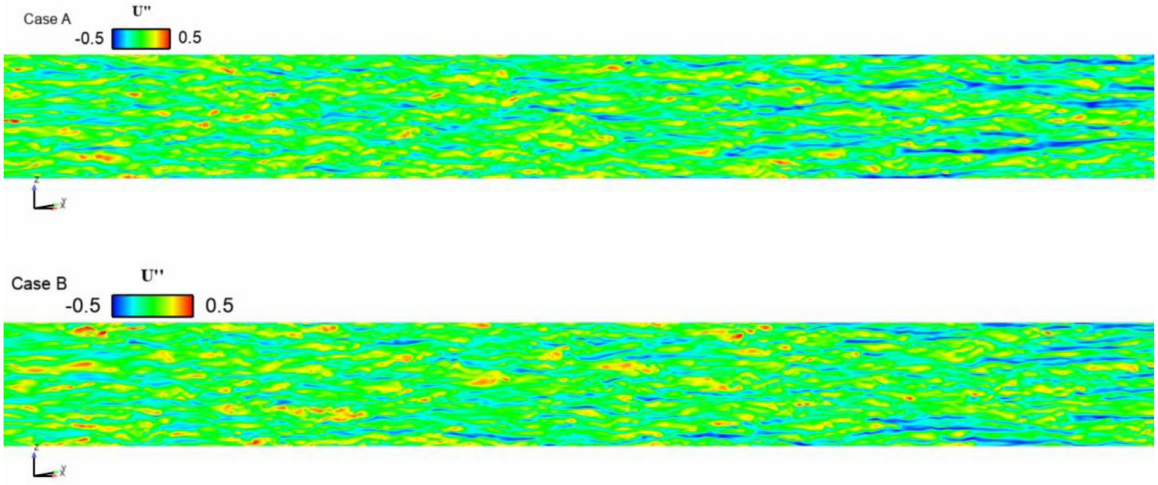

Fig. 10. The instantaneous streamwise velocity fluctuation at $y = 0.05$ or $y^+ = 10$.

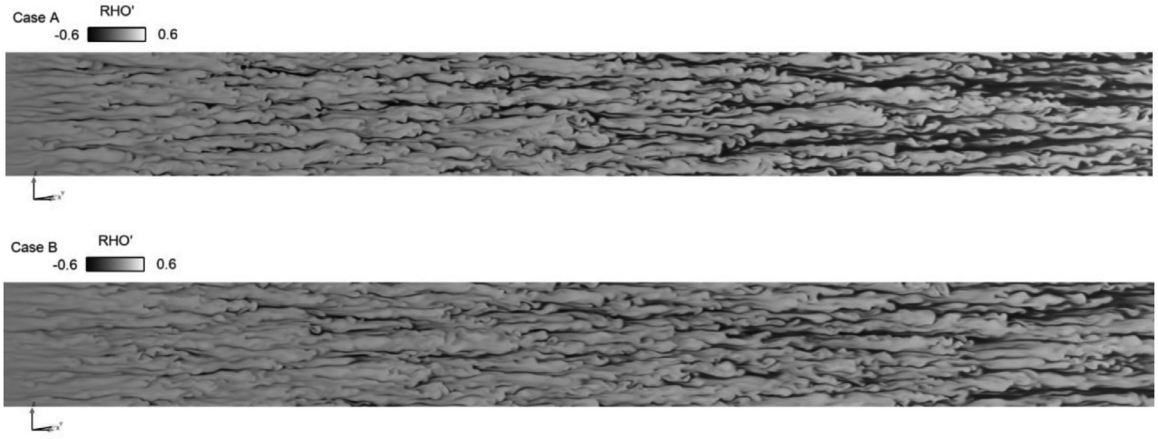

Fig. 11. The instantaneous density fluctuation at $y = 0.05$ or $y^+ = 10$.

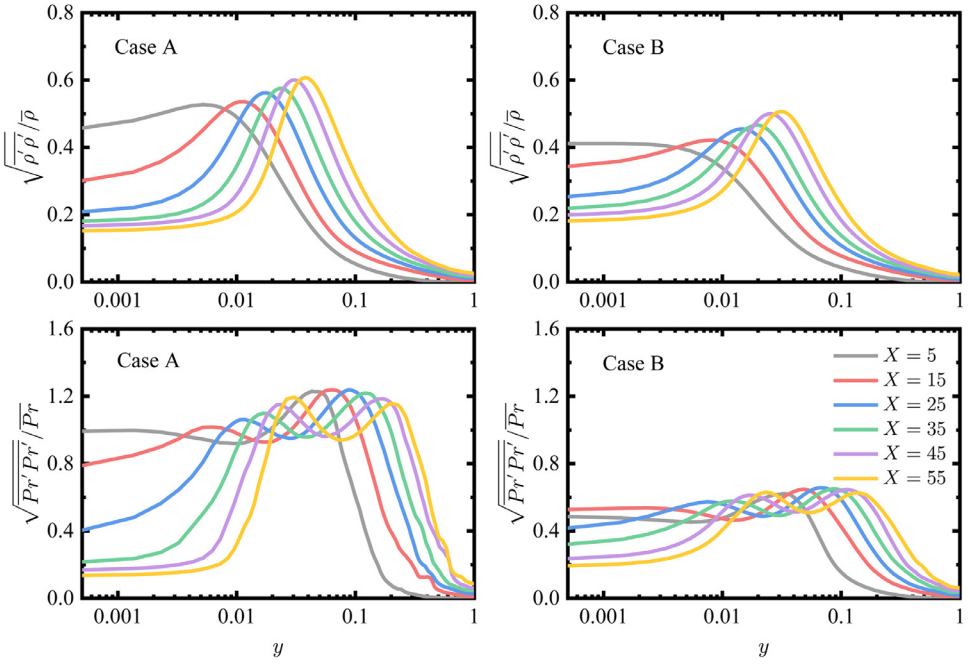

Fig. 12. Variances of density $\sqrt{\overline{\rho''\rho''}}/\bar{\rho}$ and Prandtl number $\sqrt{\overline{Pr''Pr''}}/\overline{Pr}$.

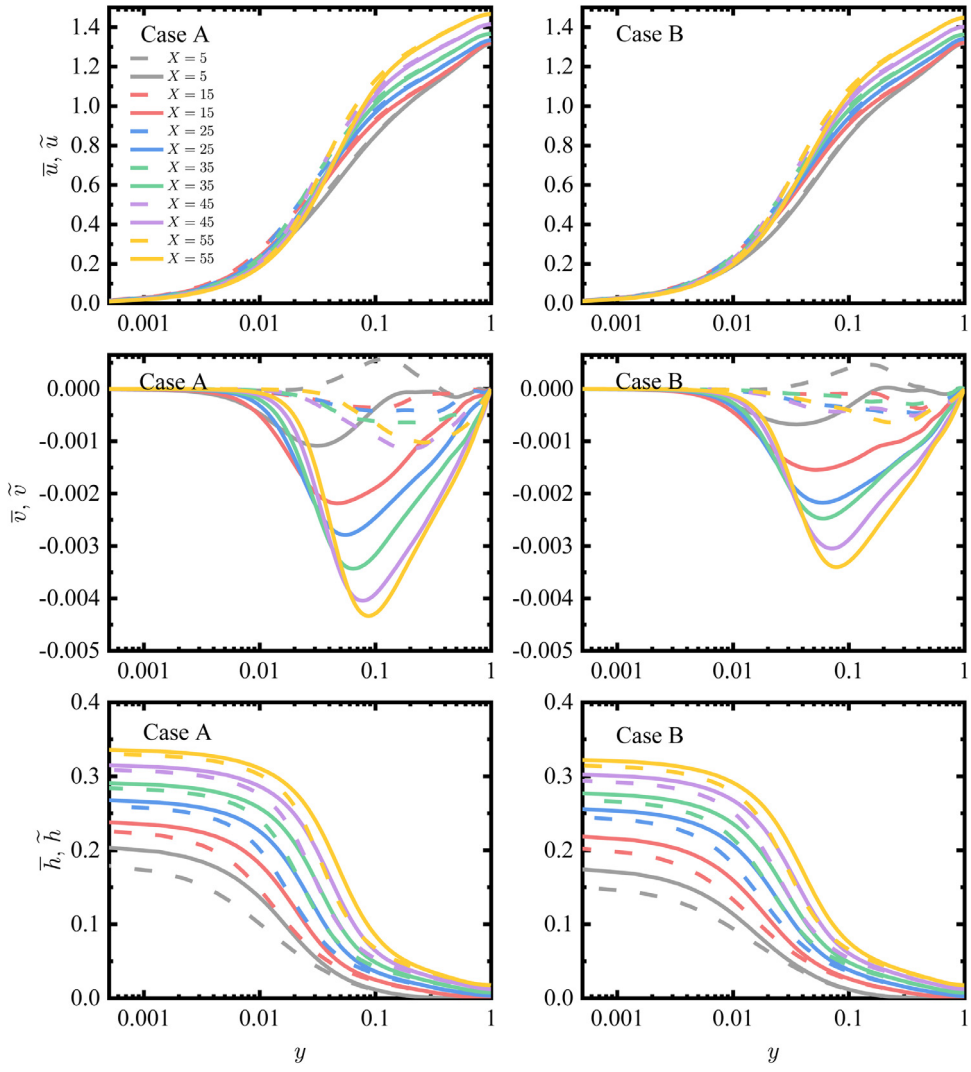

Fig. 13. The Reynolds (Solid lines) and Favred (Dashed lines) averaged mean axial velocity, radial velocity and enthalpy. (For interpretation of the references to colour in this figure legend, the reader is referred to the web version of this article.)

large property fluctuations on mean velocity, mean temperature, turbulent stress, turbulent heat flux, and near-wall turbulence scaling are discussed in detail.

3.6. Effect of large property fluctuations on turbulent statistics

The effects of density fluctuation on mean velocity and temperature are investigated. Since the Reynolds- and Favre-averaged velocities have the correlation of

$$\overline{u_i} - \widetilde{u_i} = -\overline{\rho' u'_i}/\bar{\rho} \tag{9}$$

It can be seen that the density fluctuation influences the statistics of mean velocity through the turbulent mass flux $\overline{\rho' u'_i}/\bar{\rho}$. Therefore, the difference between the Reynolds and Favre-averaged velocities can clearly show the impact of density fluctuation. From Fig. 13, though the difference between the two types of mean axial velocity is small, a remarkable difference exists for the profiles of mean radial velocity and this difference only becomes more prominent with the development of boundary layer along the streamwise direction. This suggests that in the spatial-developing turbulence at supercritical pressures, the mean turbulent mass flux $\overline{\rho' u'_i}$ is important and hence, should be modeled in RANS-based simulations.

The density fluctuation on mean enthalpy can be shown from the difference between the Reynolds- and Favre-averaged enthalpy by the correlation of

$$\bar{h} - \tilde{h} = -\overline{\rho' h'}/\bar{\rho} \tag{10}$$

It can be seen in Fig. 13 that there is an obvious difference between the Reynolds and Favre-averaged enthalpy due to the large density fluctuation. Therefore, it can be concluded that the density fluctuation is very important for the first order statistics at supercritical pressures.

The correlations between ρ' and u', v', h' are also shown in Fig. 14. The correlations increase with development of the boundary layer in the downstream due to the increase of density fluctuation. Specially, the correlations of $-\overline{\rho' h'}/\bar{\rho}$ in case A are much larger than in case B, due to the drastic Prandtl number fluctuations $\sqrt{\overline{Pr'' Pr''}}/\overline{Pr} > 1$ observed in case A as shown in Fig. 12.

To investigate the effect of density fluctuation on turbulent shear stress along the streamwise direction, we further decompose the Reynolds shear stress $-\bar{\rho}\widetilde{u''v''}$ into two terms, the mean-density-related term $-\bar{\rho}\overline{u''v''}$ and density-fluctuation-related term $-\overline{\rho' u'' v''}$ as follows

$$\frac{\widetilde{u''v''}}{\overline{u_\tau^*}^2} = \frac{\overline{u''v''}}{\overline{u_\tau^*}^2} + \frac{\overline{\rho' u'' v''}}{\bar{\rho}\overline{u_\tau^*}^2} \tag{11}$$

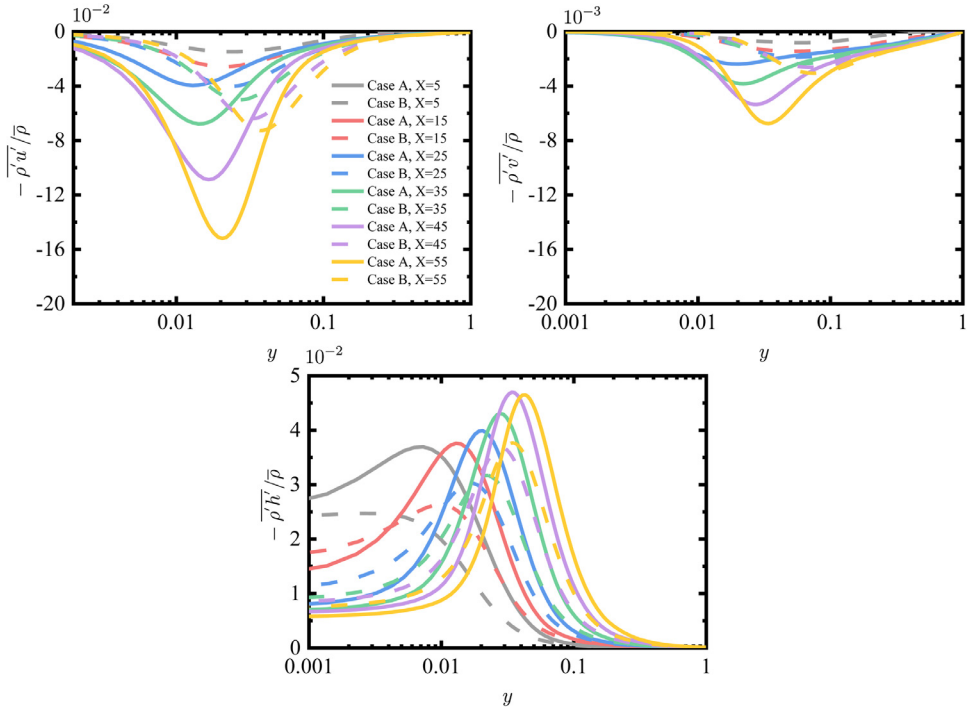

Fig. 14. Correlations between ρ' and u', v', h' ($-\overline{\rho' u_i'}/\bar{\rho}$ and $-\overline{\rho' h'}/\bar{\rho}$).

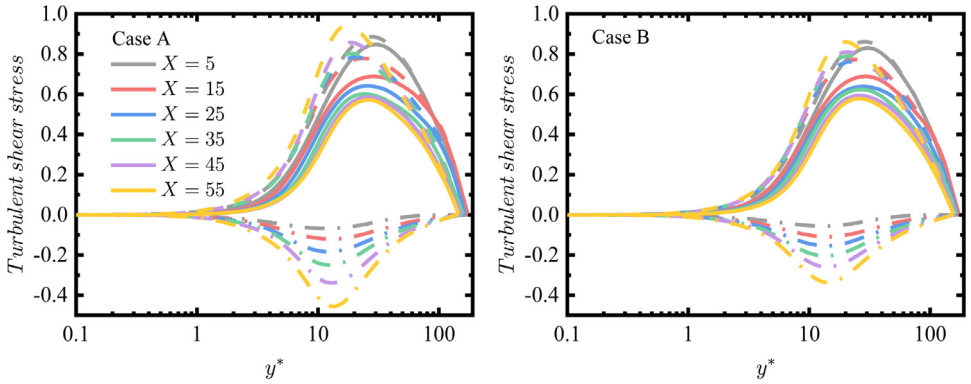

Fig. 15. The decomposed Reynolds shear stress as a function of y^*. Solid lines:Reynolds shear stress; dashed lines: mean-density-related Reynolds shear stress; dashed-dotted lines: density-fluctuation-related Reynolds shear stress.

It can be seen that the density fluctuation influences the turbulent shear stress through the density-fluctuation-related term. From Fig. 15, it can be seen that the contribution of the density-fluctuation-related term to the turbulent stress cannot be negligible compared to the mean-density-related term. Unlike the mean-density-related term, the density-fluctuation-related term makes a negative contribution to the total turbulent shear stress, which means that a large density fluctuation reduces the turbulent stress and thus, attenuates the turbulence by reducing the turbulence production $-\overline{\rho u''_i u''_j}(\frac{d\tilde{u}_j}{dx_i})$. The values of the density-fluctuation-related term in case B are a little smaller than in case A. However, a significant reduction of turbulent stresses by large density fluctuation can be observed at both supercritical pressures.

The effect of property fluctuations on turbulent heat transfer can also be shown by the following decomposition:

$$\frac{\widetilde{u''_i h''}}{q^+} = \frac{\overline{u''_i h''}}{q^+} + \frac{\overline{\rho' u''_i h''}}{\bar{\rho} q^+} \tag{12}$$

The turbulent heat fluxes on the left side can be decomposed into the mean-density-related terms $\bar{\rho}\overline{u''h''}$, $\bar{\rho}\overline{v''h''}$ and density-fluctuation-related terms $\overline{\rho' u''h''}$, $\overline{\rho' v''h''}$, respectively. The density-fluctuation-related terms show the density fluctuation on the turbulent heat flux. Fig. 16 illustrates the evolution characteristics of decomposed turbulent heat flux. It is surprising that the density-fluctuation-related terms are so important, that their absolute values are close to the mean-density-related terms. Since the density-fluctuation-related terms are opposite to mean-density-related terms, the turbulent heat fluxes are severely weakened by the large density fluctuation. Therefore, the turbulent heat transfer may be largely improved by suppressing density fluctuation at supercritical pressures.

3.7. Scaling of mean velocity and temperature

To further study the effect of large property fluctuations on near-wall turbulence, the near-wall scaling of mean velocity and temperature are discussed in detail for the spatial-developing flow. As far as we known, the commonly used scaling methods for variable density flows mainly include three kinds of velocity transformation, $\widetilde{u^+}$, $\widetilde{u^+_{VD}}$, $\widetilde{u^*}$, and two nondimensional

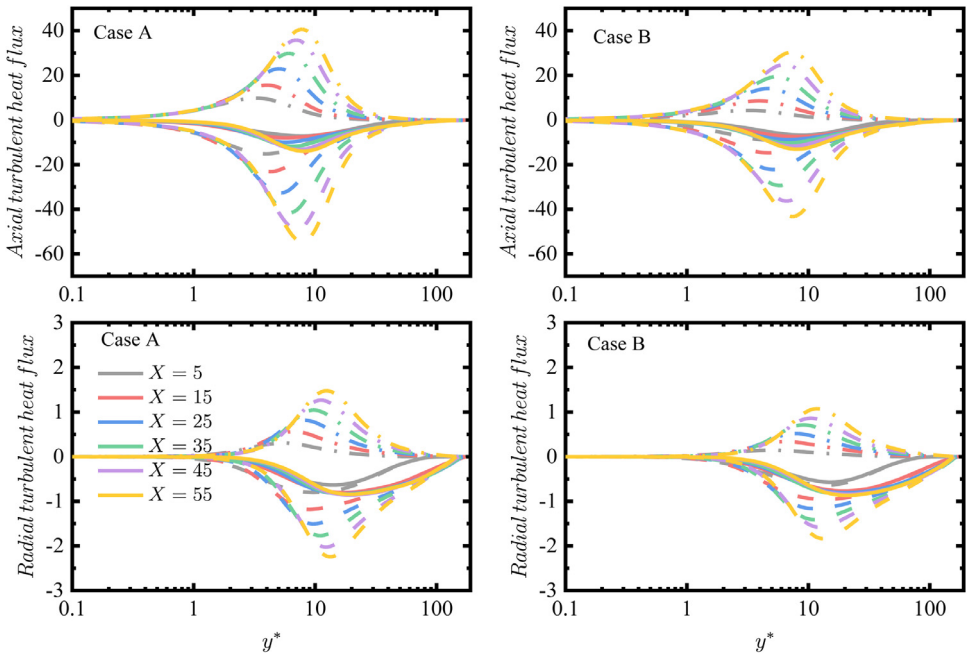

Fig. 16. The axial and radial turbulent heat fluxes. Solid lines: total; dashed lines: mean-density-related terms; dashed-dotted lines: density-fluctuation-related terms.

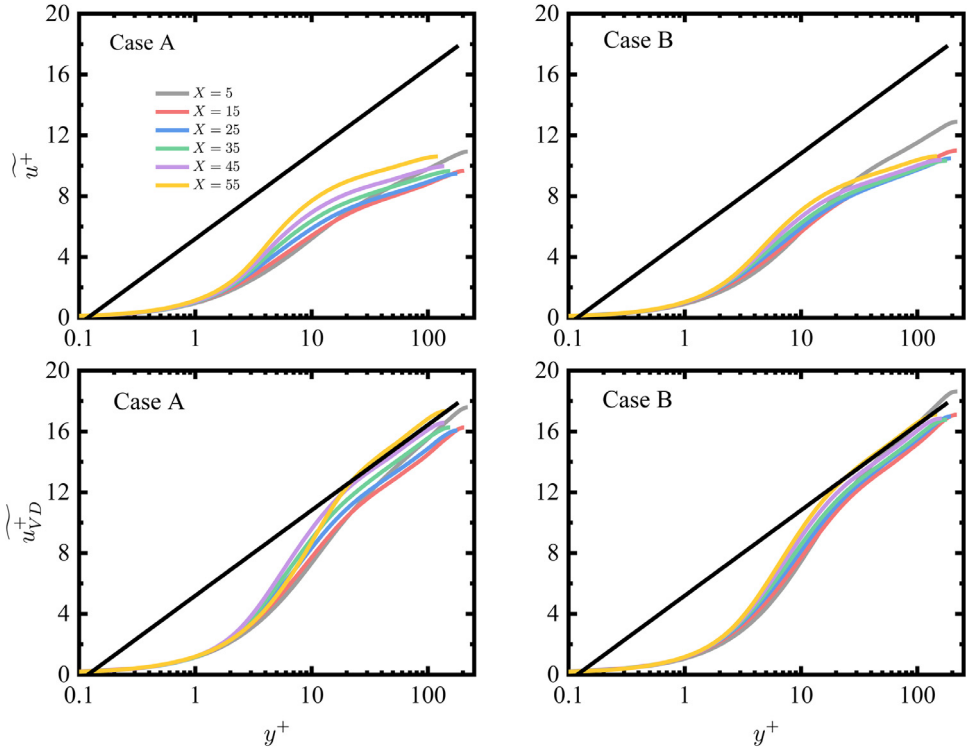

Fig. 17. The classical and van Driest velocity scalings as a function of y^+. black line: $\overline{u^+} = 2.5 * lny^+ + 5.5$.

coordinates y^+, y^*. The classical velocity transformation $\widetilde{u^+} = \tilde{u}/u_\tau$, where $u_\tau = \sqrt{\tau_w/\rho_w}$ is friction velocity, is suitable for the constant property flows. Further, Huang, Coleman, and Bradshaw [33] proposed the van Driest velocity transformation $u_{VD}^+ = \int_0^{\widetilde{u^+}} \sqrt{\bar{\rho}/\rho_w} d\widetilde{u^+}$ for variable property flows. Based on a semi-locally scaled method, the semi-local velocity transformation $\widetilde{u^*} = \int_0^{\widetilde{u_{VD}^+}} (1 + (y/Re_\tau^*) dRe_\tau^* dy) d\widetilde{u_{VD}^+}$, where $Re_\tau^* = Re_\tau \sqrt{(\bar{\rho}/\rho_w)}/(\bar{\mu}/\mu_w)$ is the semi-local Reynolds number, was derived by Trettel et al. [34] and Pecnik et al. [35]. $y^+ = y/\delta_\nu$ is the classical dimensionless wall coordinate, where $\delta_\nu = \overline{\mu_w}/\overline{\rho_w} u_\tau$ is the viscous length scale. $y^* = y/\delta_\nu^*$ is the semi-local dimensionless wall distance, where $\delta_\nu^* = \overline{\mu_w}/\overline{\rho_w} u_\tau^*$ is the semi-local viscous length scale. However, all of the mentioned scaling methods are based on the Morkovin's hypothesis, which is valid for small thermophysical property fluctuations. Therefore, the suitability of these scaling methods for the spatial-developing turbulence at supercritical pressures with large property fluctuations should be studied.

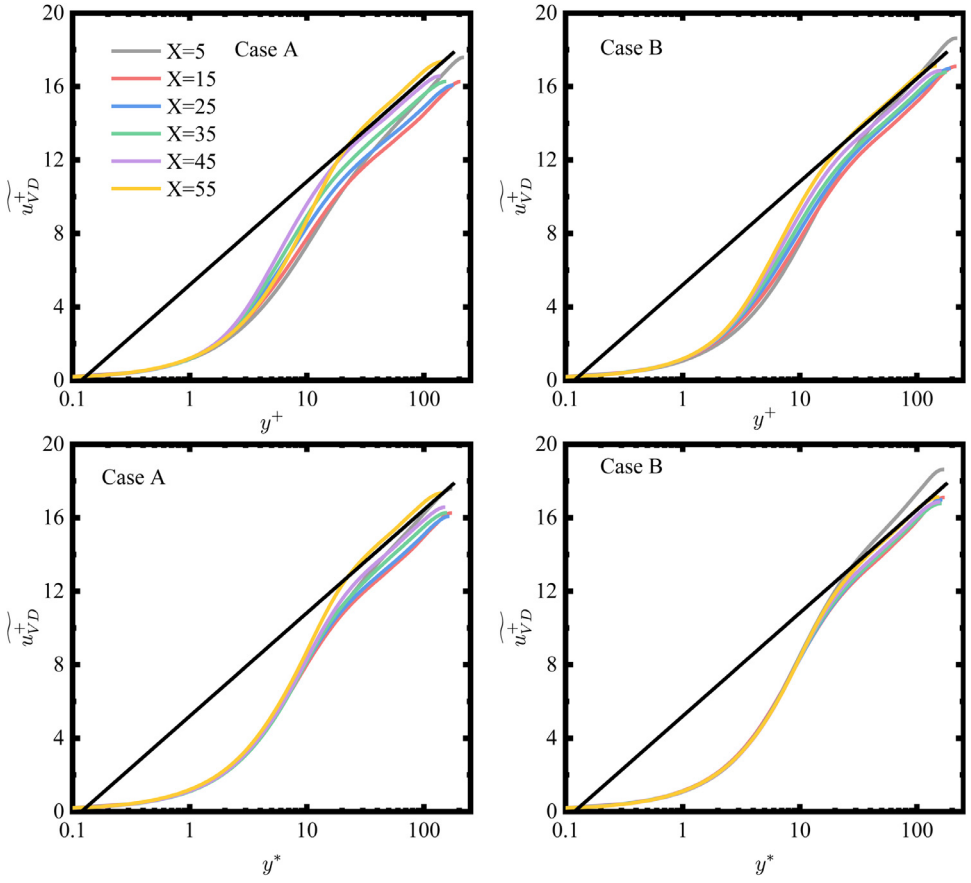

Fig. 18. The van Driest velocity scaling as a function of y^+, y^* respectively. Black line: $\overline{u^+} = 2.5 * lny^+ + 5.5$.

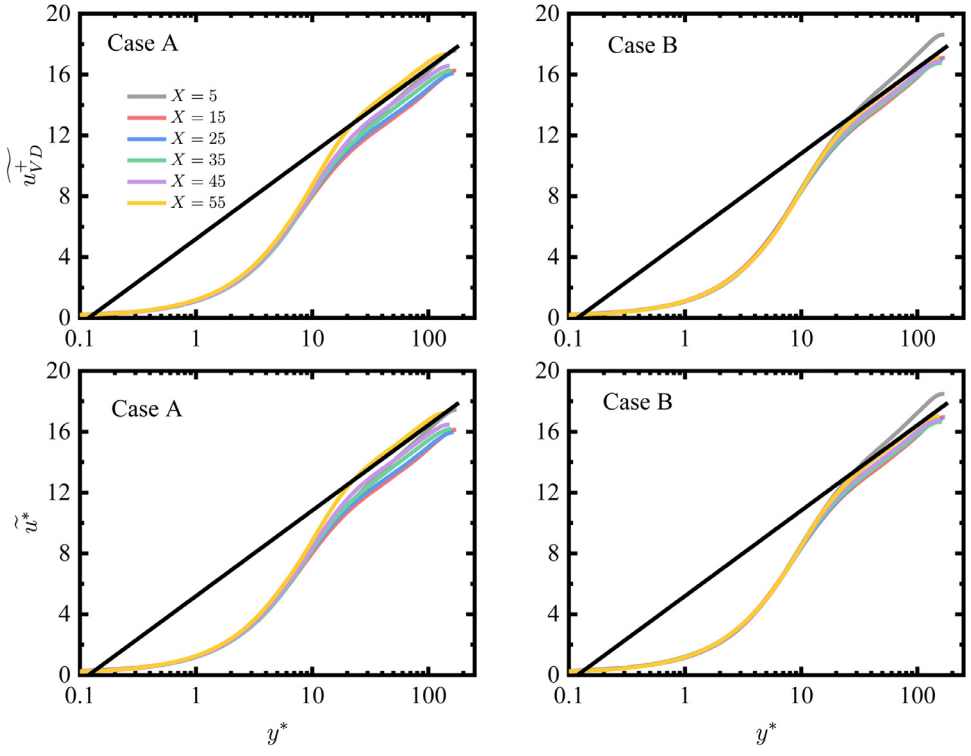

Fig. 19. The van Driest and semi-locally scaled velocity scalings as a function of y^*. Black line: $\overline{u^+} = 2.5 * lny^+ + 5.5$.

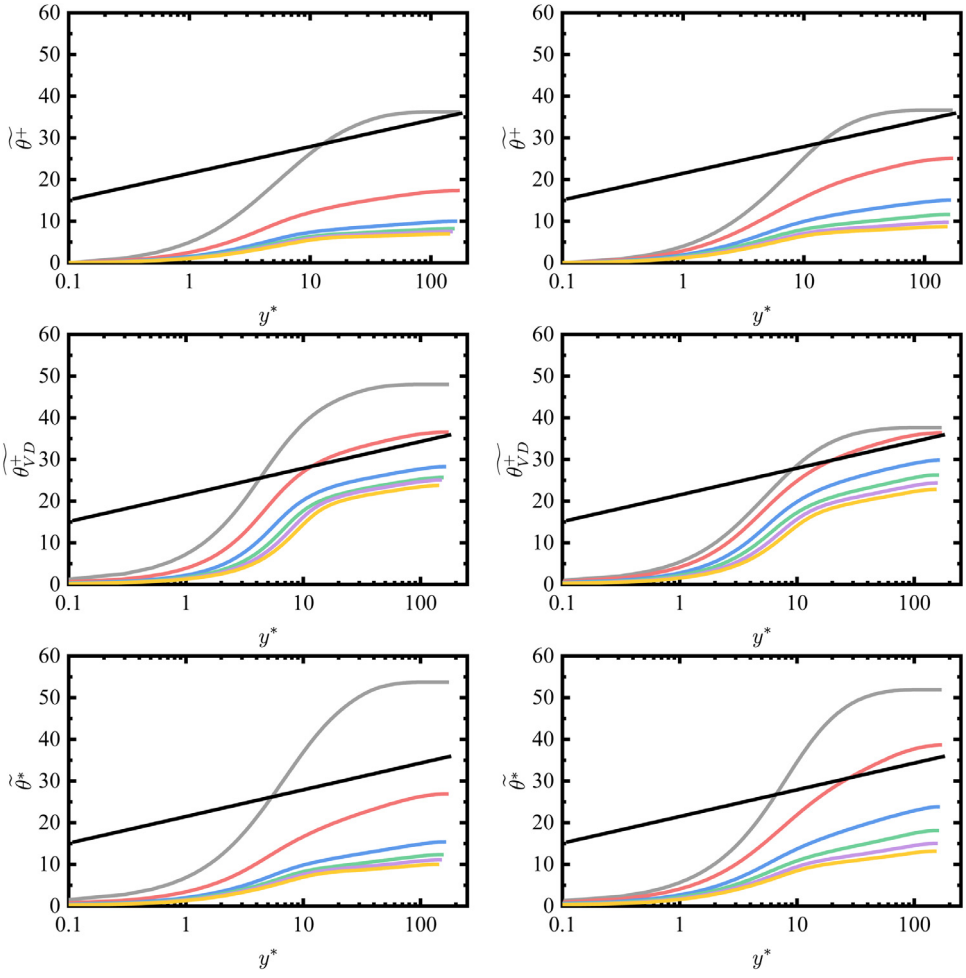

Fig. 20. The transformed mean temperature profiles as a function of y^*. Black line: $\overline{\theta^+} = 2.78 * lny^+ + 21.5$.

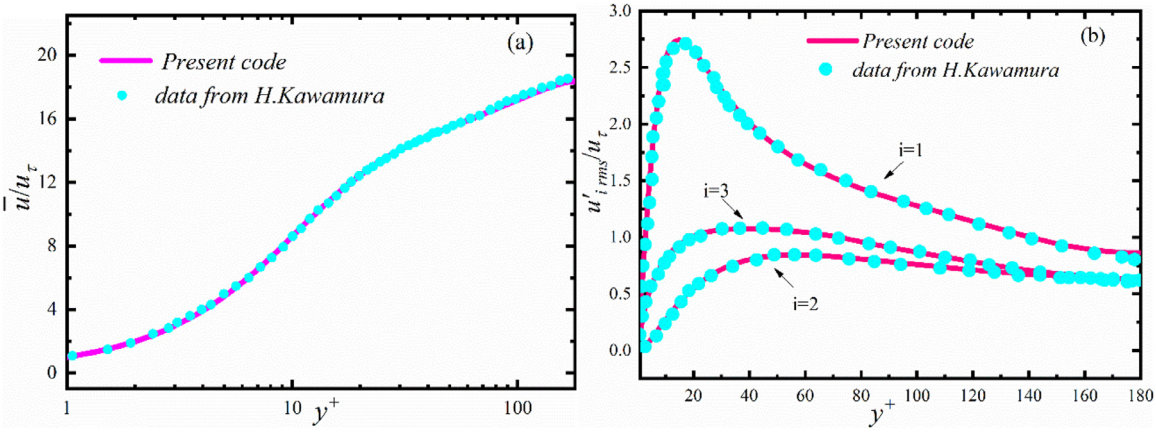

Fig. 21. (a) Mean velocity profile $\bar{u}/u_\tau$ and (b) Root-mean-square of velocity fluctuationsu'_{rms}/u_τ. Lines, present code; symbols, data obtained from Kawamura, Abe, and Shingai.

Fig. 17 shows the mean velocity transformations with classical nondimensional coordinate y^+. Apparently, classical velocity profiles of $\widetilde{u^+}$ as a function of y^+ have a disagreement with the logarithmic profile. The van Driest velocity profiles $\widetilde{u^+_{VD}}$ improve the agreement with the logarithmic profile. Considering the large mean density variation at supercritical pressures, it is reasonable to choose van Driest velocity rather than the classical $\widetilde{u^+}$ for velocity transformation. Fig. 18 shows the van Driest velocity profiles with two nondimensional coordinates y^+ and y^*. Obviously, the semi-local scaled coordinate y^* makes the van Driest velocity transformation show a better agreement in the logarithmic region.

Further, Fig. 19 plots the transformed mean velocity profiles, $\widetilde{u^+_{VD}}$ and $\widetilde{u^*}$ with the semi-local coordinate y^*. The velocity profiles from $\widetilde{u^*}$ show a better collapse, but the difference clearly keeps along streamwise direction. This means that the capability of present velocity transformations still need improvement to meet the requirement of large property fluctuations in spatial-developing turbulence at supercritical pressures.

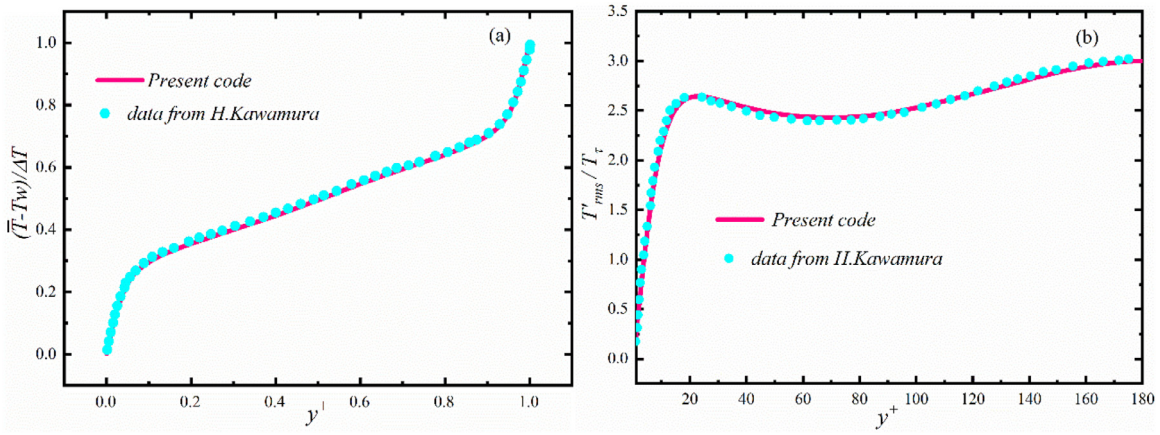

Fig. 22. (a) Mean temperature profile $(\bar{T}-T_w)/T_\tau$ and (b) Root-mean-square of temperature fluctuationsT'_{rms}/T_τ. T_τ is friction temperature defined as$T_\tau = q_w/\rho c_p u_\tau$. Lines, present code; symbols, data obtained from Kawamura, Abe, and Shingai.

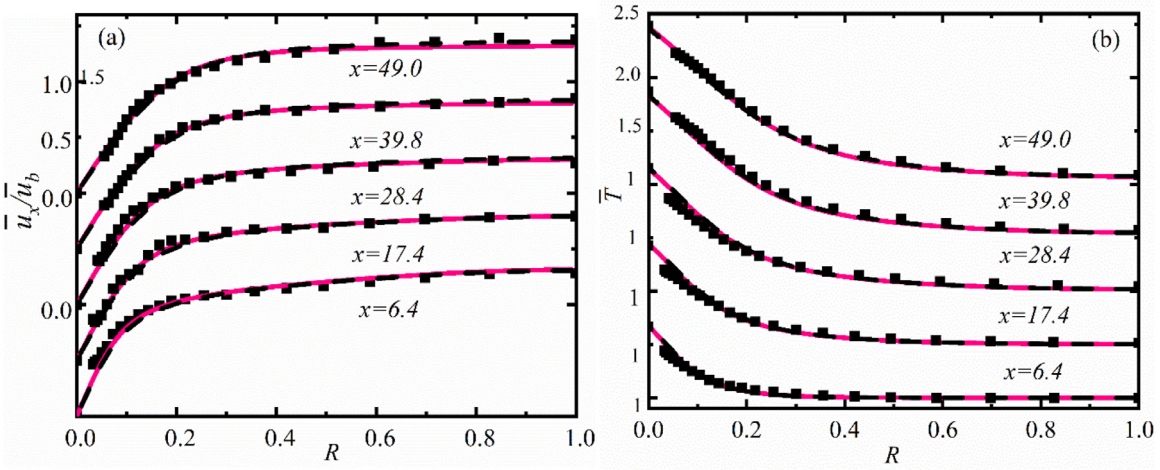

Fig. 23. (a) Mean velocity profile $\overline{u_x}/u_b$and (b) Mean velocity profile $\bar{T}$ along the radial direction. Lines, present code, with red lines, mixed convection and black dotted line, forced convection; symbols, experimental data obtained from Shehata and Mceligot.

For the temperature scaling of supercritical fluids, Bae et al. [14] firstly employed the classical temperature scaling method $\widetilde{\theta^+} = (T_w - \bar{T})/T_\tau$, where $T_\tau = q^+/(\rho_w c_{pw}\widetilde{u_\tau})$. A failure collapse of mean temperature profiles can be observed in their work. Further, Patel et al. [36] applied the van Driest transformed temperature profile $\tilde{\theta}^{VD} = \int_0^{\widetilde{\theta^+}} (\bar{\rho}/\rho_w)^{1/2} d\widetilde{\theta^+}$ to derive an extended van Driest transformation $\widetilde{\theta^*} = \int_0^{\tilde{\theta}^{VD}} [1 + (y/Re_\tau^*) dRe_\tau^*/dy] d\tilde{\theta}^{VD}$for variable density flows. This transformation does not consider the large variation of specific heat. However, as shown in Fig. 1, the variation of specific heat at supercritical pressures is so drastic that it causes large variations of mean Prandtl number and its fluctuation. This impact should be incorporated in the temperature transformation. Therefore, a modified van-Direst transformation $\widetilde{\theta^+_{VD}} = \int_0^{\widetilde{\theta^+}} (\bar{\rho}\overline{c_p}/\rho_w c_{pw})^{1/2} d\widetilde{\theta^+}$ including the local specific heat was given here. Fig. 20 shows the different temperature transformations, $\widetilde{\theta^+}$, $\widetilde{\theta^+_{VD}}$ and $\widetilde{\theta^*}$ with the semi-local y^* coordinate for case A and B. The van Driest transformed temperature profiles $\widetilde{\theta^+_{VD}}$ which take into account the effects of mean density and specific heat, show a better logarithmic distribution. However, a large deviation still exists and this may be due to the large fluctuations of Prandtl number in turbulent heat transfer at supercritical pressures, because all

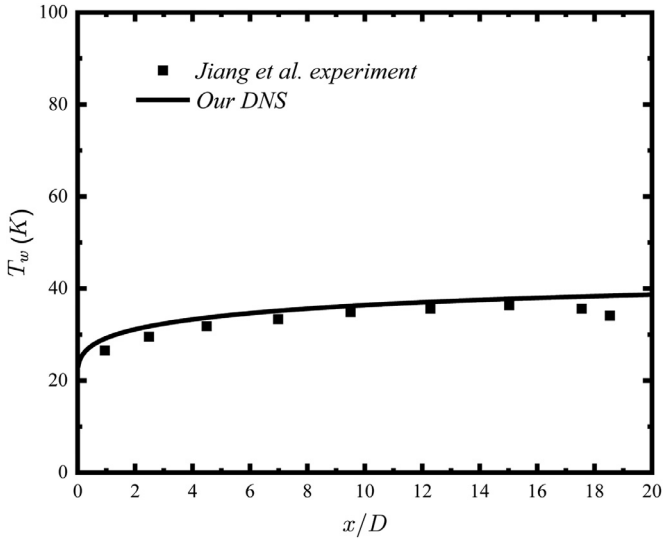

Fig. 24. Local wall temperatures for upward flow P = 8.85 MPa, T_0= 293.65 K, Re = 1700, q_w=5.3kw/m^2.

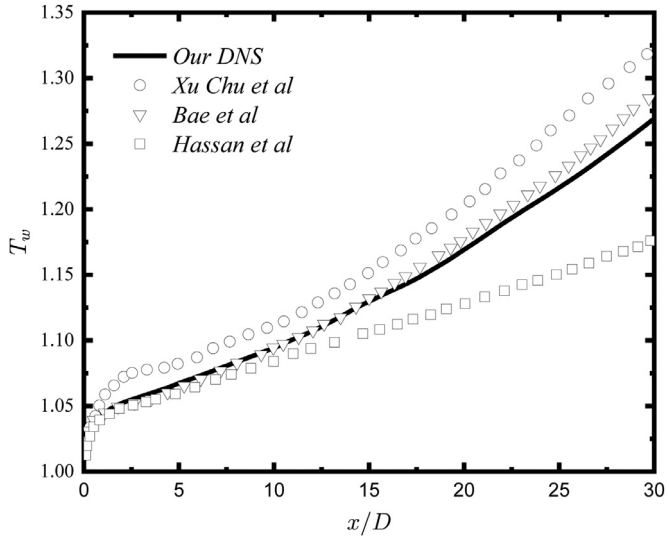

Fig. 25. The wall temperatures calculated by our code compared with the results of Bae et al., Xu et al. and Hassan et al.

the transformations only incorporate the local mean thermophysical properties and cannot consider their fluctuations.

4. Conclusion

Direct numerical simulations of turbulent heat transfer of supercritical fluids in a spatial-developing pipe with constant heat flux have been conducted. The characteristics and mechanisms of turbulent flow and heat transfer were comprehensively analyzed at different supercritical pressures. Different analytical methods, such as first-order and second-order statistics, FIK decompositions, flow visualizations etc. are used. The major conclusions that can be drawn are as follows:

1) Both the skin friction coefficient and Nusselt number decrease at supercritical pressures due to large thermophysical property variations, which leads to a large increase of wall temperatures in heat transfer of supercritical fluids. Furthermore, with the smaller pressure ratio, skin friction coefficient and Nusselt number decrease faster due to the more drastic property variations.
2) The FIK decompositions show that the decrease of skin friction coefficient and Nusselt number at supercritical pressures is mainly due to the large turbulence reduction. The analyses of the turbulent kinetic energy (TKE), turbulent shear stress, the production of TKE also confirm this point.
3) The thermophysical property fluctuations are very large and this influences the turbulence and heat transfer significantly. The correlations between ρ' and u', v', h' are all significant and cannot be negligible. The density-fluctuation-related terms are large and even comparable to the mean-density-related terms. The density-fluctuation-related terms have a negative contribution to turbulent shear stress and turbulent heat flux, which leads to the decrease in skin friction coefficient and Nusselt number.
4) For near-wall scaling of mean velocity and temperature in spatial-developing flows at supercritical pressures, the semi-local velocity transformation with a semi-local nondimensional coordinate shows a better agreement in the logarithmic region, while the modified van Direst transformation is better for mean temperature. However, a clear deviation still exists especially for mean temperature because all the transformations only incorporate the local mean thermophysical properties and cannot consider their fluctuations.

Declaration of Competing Interest

We declare that we have no financial and personal relationships with other people or organizations that can inappropriately influence our work, there is no professional or other personal interest of any nature or kind in any product, service or company that could be construed as influencing the position presented in, or the review of, the manuscript entitled, “Numerical investigation of spatial-developing turbulent heat transfer of supercritical fluids at different supercritical pressures”.

Acknowledgments

This work is financially supported by the Collaborative Innovation Program of Hefei Science Center, CAS (2019HSC–CIP006) and the National Key Research and Development Program of China (2017YFE0300500, 2017YFE0300503). The numerical calculations in this paper have been conducted on the supercomputing system in the Supercomputing Center of the University of Science and Technology of China (USTC).

Appendix A. Validation

1) Verification of constant property flows

Our code was firstly verified with the DNS data from Kawamura, Abe, and Shingai [37]. Fig. 21(a) and 21(b) compare our DNS data [38] with those of Kawamura, Abe, and Shingai [37] for mean velocity and root-mean-square of velocity fluctuations at $Re_\tau = 180$ and $Pr_w = 0.71$, respectively. Fig. 22(a) and 22(b) show similar comparison for mean temperature and root-mean-square of temperature fluctuations. As can be seen, all statistics show an excellent agreement with Kawamura Abe, and Shingai [37].

2) Validation of the strong heated air flows with variable properties

The computational method was also validated by a strong heated air flow with experimental data [39]. Fig. 23(a) and 23(b) compare the mean velocity and temperature profiles from our DNS data [21] with the experimental data from Shehata and Mceligot. An excellent agreement of all statistics is also reached. More details can be found in the reference [21].

3) Validation of laminar supercritical CO_2 flows

In order to validate the code with experimental data for supercritical fluids, we compared the DNS results with experimental data of supercritical CO2 at Re=1700 (Jiang et al. [40]). It was found that the calculated wall temperatures have a good agreement with the experimental data as shown in Fig. 24.

4) Validation of turbulent supercritical CO_2 flows

The DNS code was also validated with other DNS results for supercritical CO2 turbulent heat transfer. The case B from Bae et al. [13] was calculated and compared. Xu et al. [41] and Hassan et al. [15] also performed the same case. From the Fig. 25, the wall temperatures calculated by our code show a good agreement with those of Bae et al. [13]. The difference of our DNS and Hassan et al. may be due to the different thermophysical property data.

References

[1] J. Yoo, Y. Ishiwatari, Y. Oka, J. Liu, Conceptual design of compact supercritical water-cooled fast reactor with thermal hydraulic coupling, Ann Nucl Energy 33 (11–12) (2006) 945–956.

[2] I.L. Pioro, R.B. Duffey, Experimental heat transfer in supercritical water flowing inside channels (survey), Nucl Eng Des 235 (22) (2005) 2407–2430.
[3] I.L. Pioro, H.F. Khartabil, R.B. Duffey, Heat transfer to supercritical fluids flowing in channels—Empirical correlations (survey), Nucl Eng Des 230 (1–3) (2004) 69–91.
[4] H. Swenson, J. Carver, C.d. Kakarala, Heat transfer to supercritical water in smooth-bore tubes, J Heat Transfer 87 (4) (1965) 477–483.
[5] K. Yamagata, K. Nishikawa, S. Hasegawa, T. Fujii, S. Yoshida, Forced convective heat transfer to supercritical water flowing in tubes, Int J Heat Mass Transf 15 (12) (1972) 2575–2593.
[6] Y.Y. Bae, Mixed convection heat transfer to carbon dioxide flowing upward and downward in a vertical tube and an annular channel, Nucl Eng Des 241 (8) (2011) 3164–3177.
[7] J. Wang, H. Li, B. Guo, S. Yu, Y. Zhang, T. Chen, Investigation of forced convection heat transfer of supercritical pressure water in a vertically upward internally ribbed tube, Nucl Eng Des 239 (10) (2009) 1956–1964.
[8] J. Wang, H. Li, S. Yu, T. Chen, Investigation on the characteristics and mechanisms of unusual heat transfer of supercritical pressure water in vertically-upward tubes, Int J Heat Mass Transf 54 (9–10) (2011) 1950–1958.
[9] M. Zhao, H.Y. Gu, X. Cheng, Experimental study on heat transfer of supercritical water flowing downward in circular tubes, Ann Nucl Energy 63 (2014) 339–349.
[10] H.Y. Gu, M. Zhao, X. Cheng, Experimental studies on heat transfer to supercritical water in circular tubes at high heat fluxes, Experimental Thermal and Fluid Science 65 (2015) 22–32.
[11] Z.B. Liu, Y.-L. He, Y.-F. Yang, J.-Y. Fei, Experimental study on heat transfer and pressure drop of supercritical CO2 cooled in a large tube, Appl Therm Eng 70 (1) (2014) 307–315.
[12] D. Huang, B. Ruan, X. Wu, W. Zhang, G. Xu, Z. Tao, P. Jiang, L. Ma, W. Li, Experimental study on heat transfer of aviation kerosene in a vertical upward tube at supercritical pressures, Chin. J. Chem. Eng. 23 (2) (2015) 425–434.
[13] J.H. Bae, J.Y. Yoo, H. Choi, Direct numerical simulation of turbulent supercritical flows with heat transfer, Physics of Fluids 17 (10) (2005) 105104.
[14] J.H. Bae, J.Y. Yoo, D.M. McEligot, Direct numerical simulation of heated CO2 flows at supercritical pressure in a vertical annulus at *Re*=8900, Physics of Fluids 20 (5) (2008) 055108.
[15] H. Nemati, A. Patel, B.J. Boersma, R. Pecnik, Mean statistics of a heated turbulent pipe flow at supercritical pressure, Int J Heat Mass Transf 83 (2015) 741–752.
[16] X. Chu, E. Laurien, Flow stratification of supercritical CO2 in a heated horizontal pipe, J Supercrit Fluids 116 (2016) 172–189.
[17] S. Pandey, X. Chu, E. Laurien, B. Weigand, Buoyancy induced turbulence modulation in pipe flow at supercritical pressure under cooling conditions, Physics of Fluids 30 (6) (2018).
[18] J.W.R. Peeters, R. Pecnik, M. Rohde, T.H.J.J. van der Hagen, B.J. Boersma, Characteristics of turbulent heat transfer in an annulus at supercritical pressure, Physical Review Fluids 2 (2) (2017).
[19] W.R. Jurriaan, R. Peeters, M. Pecnik, T.H. Rohde, J.J. van der Hagen, B.J. Boersma, Turbulence attenuation in simultaneously heated and cooled annular flows at supercritical pressure, J Fluid Mech 799 (2016) 505–540.
[20] S. Kawai, Heated transcritical and unheated non-transcritical turbulent boundary layers at supercritical pressures, J Fluid Mech 865 (2019) 563–601.
[21] P. Zhao, J. Liu, Z. Ge, Y. Li, N. Zhao, Y. Wan, Direct numerical simulation of strongly heated air flows in a vertical pipe using a thermophysical property table, Int J Heat Mass Transf 124 (2018) 1181–1197.
[22] P. Zhao, J. Zhu, Z. Ge, J. Liu, Y. Li, Direct numerical simulation of turbulent mixed convection of LBE in heated upward pipe flows, Int J Heat Mass Transf 126 (2018) 1275–1288.
[23] J. Liu, Y. Jin, P. Zhao, Z. Ge, Y. Li, Y. Wan, Analysis of heat transfer of supercritical water by direct numerical simulation of heated upward pipe flows, International Journal of Thermal Sciences 138 (2019) 206–218.
[24] E.W. Lemmon, M.L. Huber, M.O. McLinden, NIST reference fluid thermodynamic and transport properties–REFPROP, NIST standard reference database 23 (2002) v7.
[25] F. Zonta, C. Marchioli, A. Soldati, Modulation of turbulence in forced convection by temperature-dependent viscosity, J Fluid Mech 697 (2012) 150–174.
[26] J. Lee, S. Yoon Jung, H. Jin Sung, T.A. Zaki, Effect of wall heating on turbulent boundary layers with temperature-dependent viscosity, J Fluid Mech 726 (2013) 196–225.
[27] H. Nemati, A. Patel, B.J. Boersma, R. Pecnik, The effect of thermal boundary conditions on forced convection heat transfer to fluids at supercritical pressure, J Fluid Mech 800 (2016) 531–556.
[28] F. Chambers, H. Murphy, D. McEligot, Laterally converging flow. Part 2. Temporal wall shear stress, J Fluid Mech 127 (1983) 403–428.
[29] K. Fukagata, K. Iwamoto, N. Kasagi, Contribution of Reynolds stress distribution to the skin friction in wall-bounded flows, Physics of Fluids 14 (11) (2002) L73–L76.
[30] K. Fukagata, N. Kasagi, Drag reduction in turbulent pipe flow with feedback control applied partially to wall, International Journal of Heat and Fluid Flow 24 (4) (2003) 480–490.
[31] T. Gomez, V. Flutet, P. Sagaut, Contribution of Reynolds stress distribution to the skin friction in compressible turbulent channel flows, Phys Rev E 79 (3) (2009) 035301.
[32] Y. Kametani, K. Fukagata, Direct numerical simulation of spatially developing turbulent boundary layers with uniform blowing or suction, J Fluid Mech 681 (2011) 154–172.
[33] P.G. Huang, G.N. Coleman, P. Bradshaw, Compressible turbulent channel flows: DNS results and modelling, J Fluid Mech 305 (–1) (2006) 185.
[34] A. Trettel, J. Larsson, Mean velocity scaling for compressible wall turbulence with heat transfer, Physics of Fluids 28 (2) (2016) 026102.
[35] R. Pecnik, A. Patel, Scaling and modelling of turbulence in variable property channel flows, Journal of Fluid Mechanics, 823 (2017).
[36] A. Patel, B.J. Boersma, R. Pecnik, Scalar statistics in variable property turbulent channel flows, Physical Review Fluids 2 (8) (2017).
[37] H. Kawamura, H. Abe, K. Shingai, DNS of turbulence and heat transport in a channel flow with different Reynolds and Prandtl numbers and boundary conditions, Turbulence, Heat and Mass Transfer 3 (2000) 15–32.
[38] T. Wan, P. Zhao, J. Liu, C. Wang, M. Lei, Mean velocity and temperature scaling for near-wall turbulence with heat transfer at supercritical pressure, Physics of Fluids 32 (5) (2020) 055103.
[39] A.M. Shehata, D.M. Mceligot, Mean structure in the viscous layer of strongly-heated internal gas flows. Measurements„ International Journal of Heat & Mass Transfer 41 (24) (1998) 4297–4313.
[40] P.-X. Jiang, Y. Zhang, Y.-J. Xu, R.-F. Shi, Experimental and numerical investigation of convection heat transfer of CO2 at supercritical pressures in a vertical tube at low Reynolds numbers, International Journal of Thermal Sciences 47 (8) (2008) 998–1011.
[41] X. Chu, E. Laurien, Investigation of convective heat transfer to supercritical carbon dioxide with direct numerical simulation, in: High Performance Computing in Science and Engineering´15, Springer, 2016, pp. 315–331.